

Article

Phosphate Mine Tailing Recycling in Membrane Filter Manufacturing: Microstructure and Filtration Suitability

Mohamed Loutou ^{1,*}, Wafa Misrar ^{2,3}, Mohammed Koudad ^{1,4}, Mohammed Mansori ², Liga Grase ⁵, Claude Favotto ⁶, Yassine Taha ⁷ and Rachid Hakkou ^{2,7}

¹ Département de Chimie, Faculté Pluridisciplinaire de Nador, Université Mohammed 1er, B.P. 300, Selouane, Nador 62700, Morocco; koudad.mohammed@yahoo.fr

² LCME, Laboratoire de Chimie des Matériaux et d'Environnement, Faculté des Sciences et Techniques, Université Cadi Ayyad, Av. A. Khattabi, B.P. 549, Marrakech 40000, Morocco; misrar.wafa@gmail.com (W.M.); m.mansori@uca.ac.ma (M.M.); r.hakkou@uca.ma (R.H.)

³ LMCN, Laboratoire de Matière Condensée et Nanostructures, Faculté des Sciences et Techniques, Université Cadi Ayyad, B.P. 549, Marrakech 40000, Morocco

⁴ Laboratory of Applied Chemistry & Environment, Faculty of Sciences, Mohammed First University, Oujda 60000, Morocco

⁵ Institute of Silicate Materials, Faculty of Materials Science and Applied Chemistry, Riga Technical University, P. Valdena 3/7, LV-1048 Riga, Latvia; grase.liga@gmail.com

⁶ IM2NP, Institut Matériaux Microélectronique Nanosciences de Provence, Université de Toulon, Bât R, BP 20132-83957, La Garde-Cedex, France; claude.favotto@univ-tln.fr

⁷ Materials Science and Nano-engineering Department, Mohammed VI Polytechnic University (UM6P), Lot 660-Hay Moulay Rachid, Bengurir, Morocco; yassine.taha@um6p.ma

* Correspondence: mohamedloutou@yahoo.fr; Tel.: +212-672-057-790

Received: 20 February 2019; Accepted: 21 May 2019; Published: 24 May 2019



Abstract: Ceramic membrane filters based on industrial by-products can be considered to be a valorization alternative of phosphate mine tailings, even more so if these ceramic membranes are used in the industrial wastewater treatment due to their good mechanical, chemical, and thermal resistance. The depollution of textile industry rejections with this method has not been studied in detail previously. In this work, ceramic membrane filters have been manufactured from natural clay and phosphate mine tailings (phosphate sludge). Blends of the abovementioned materials with a pore-forming agent (sawdust, up to 20 wt. %) were investigated in the range 900–1100 °C using thermal analysis, X-ray diffraction, scanning electron microscopy, and mercury porosimetry. Ceramic properties were measured as a function of firing temperature and sawdust addition. Filtration tests were carried out on samples with advantageous properties. The results showed that gehlenite together with diopside neofomed from lime decomposed carbonates and breakdown products of clay minerals, while calcium phosphate derived from partial decomposition of fluorapatite. Both quartz and fluorapatite resisted heating. The results of the experimental design showed that the variations of physical properties versus processing factors were well described by the polynomial model. Filtration results are quite interesting, allowing these membranes to be used in industrial effluent treatment.

Keywords: ceramic membrane; phosphate mine tailings; industrial waste; filtration; experimental design

1. Introduction

In recent years, ceramic filtering membranes have been used in a wide range of applications and processes such as biotechnology, pharmaceuticals, the food industry, and industrial effluent

treatment [1–4]. The growing interest that membrane filters has received is linked to their thermal, chemical, and mechanical properties. These remarkable properties offer ceramic membranes a large advantage over their polymeric [5,6] and metallic counterparts. However, they are usually more expensive than those based on polymers. In this respect, research on new ceramic materials that are cheaper for membrane filter manufacturing should benefit from extensive use of membrane technology, especially in developing countries, where many environmental issues should be addressed at low cost.

Micaceous clay and phosphate sludge obtained from clay deposits and phosphate-discharge plant dams (Morocco) respectively [7,8] could be a suitable material for low-cost membrane manufacture [9,10]. In fact, this method presents the advantage of allowing the substitution of the materials commonly used in this field (alumina, zirconia, cordierite, mullite etc.) [11–15] by other, less expensive ones (clay) that have similar properties. Also, there is the fact that it is an excellent way of managing industrial waste, which may constitute a potential source of pollution [8]. It has been logged that significant amounts of the abovementioned waste can be used in some specific and/or common applications, such as lightweight aggregates [16], soil amendments [17], or even construction [18].

Several scientific works have been performed regarding the incorporation of aluminosilicate-based materials in the filtration membrane manufacture [19–24]. The nature of the raw material though affects both physical and chemical properties of the final ceramic product. These properties can be tailored for each particular application by controlling the chemical and mineralogical compositions [25], and the microstructure of the used materials and additives. Despite this, little attention has been given to the use of natural pore-forming agents (lime [26], starch [27,28], wood [29], organic waste (paper from the paper industry) [30], sawdust from the woodworking industry [31–33], etc.).

This study is devoted to investigating the feasibility of the manufacture of new ceramic membrane filters from natural micaceous clay and industrial by-product (phosphate sludge). These membranes are designed to be used in industrial effluent treatment.

2. Materials and Experimental Techniques

2.1. Materials

The starting raw materials used in this research were a naturally occurring clay (SA) and phosphate waste (PS). The micaceous clay was extracted from a clay stratum in the region of Safi (Morocco) known by the pottery industry. Phosphate waste was obtained from phosphate sludge ponds generated from beneficiation plants of Moroccan phosphate rocks (Youssoufia, Morocco). The mineralogical compositions of the abovementioned materials are provided in Table 1 and Figure 1, respectively. SA consisted of hydro-muscovite (25 wt. %), quartz (12 wt. %), and dolomite (63 wt. %). PS was composed of quartz (17 wt. %), fluorapatite (44 wt. %), calcite (15 wt. %), dolomite (7 wt. %), and a smectite clay mineral (7 wt. %).

Cedar sawdust (SC) was used in this study as a pore-forming agent. It was supplied by a local carpentry factory (Marrakech, Morocco). All the raw materials used were sieved through a gyratory sieve (100 μm).

Table 1. Mineralogical compositions (wt. %) of studied raw materials. SA: Micaceous raw clay and PS: phosphate sludge. F: Fluorapatite, Q: Quartz, C: Calcite, M: Muscovite, D: Dolomite.

	Mineralogical Composition				
	F	Q	D	C	M
PS	44	17	7	15	-
SA	-	12	63	-	25

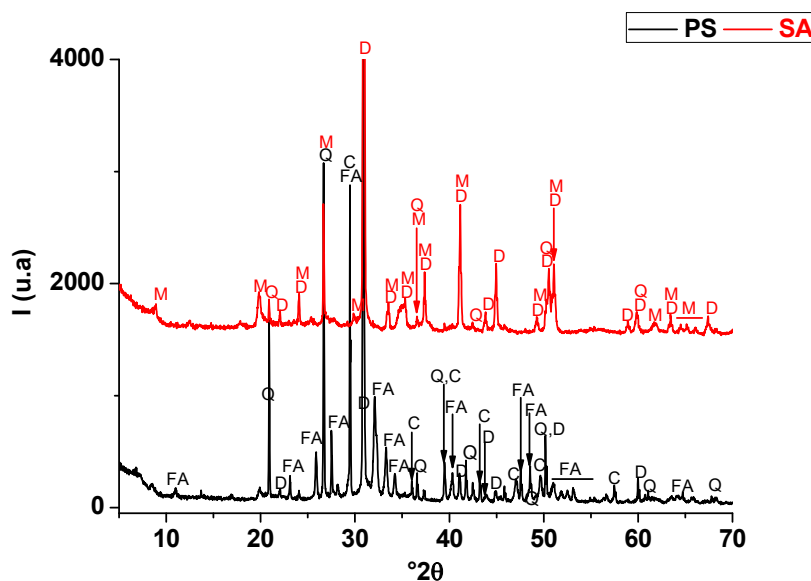


Figure 1. X-ray diffraction patterns of phosphate sludge (PS) and a dolomite-rich clay (SA). FA: fluorapatite (PDF #71-0880); Q: quartz (PDF # 5-0490); D: dolomite (PDF # 83-1766); C: calcite (PDF # 72-1650); M: Muscovite (PDF # 43-0685).

2.2. Experimental Techniques

Two binary mixtures (SA-SC (up to 20 wt. % of SC) and PS-SC (up to 20 wt. % of SC)) and a ternary one (clay-phosphate sludge-sawdust (SA:PS = 50:50 and up to 20 wt. % of SC)) were prepared for the present study. The materials were dry blended in a mortar before being moistened with tap water (10 wt. % moisture) to have consistent and comparable specimen. The mixtures were then shaped into cylindrical form ($D = 40$ mm and $h = 3$ mm) for the filtration tests and prismatic ($L = 60$ mm, $W = 10$ mm and $h = 5$ mm) for the mechanical properties, and this using an uniaxial laboratory-type pressing in a suitable mold (compression pressure = 2 tons). As reference, pore-forming agent-free samples have been prepared. The samples were heated starting from room temperature in an electric furnace (Nabertherm) at a rate of 5 °C/min in the range 900 – 1100 °C for 4 h and then cooled to room temperature in the switched-off furnace.

Samples of the heated blends were analyzed with X-ray diffraction (XRD) using an Empyrean PANalytical diffractometer operating with copper radiation ($K\alpha(\text{Cu}) = 1.5418$ Å). Quantitative mineralogical analysis was performed using the RIR method (reference intensity ratio). The thermal analysis was performed by a Setaram Setsys 24 apparatus (atmosphere: air; heating rate: 10 °C/min, reference material: Alumina). The morphological features of the blends were studied on fracture surfaces sputtered with Cr by a Schottky field emission scanning electron microscope (FE-SEM) (Nova NanoSEM 650, FEI Company, Eindhoven, The Netherlands) coupled with an energy dispersive spectroscopy (EDS) (TEAM™ integrated EDS with an Apollo X silicon drift detector) for quantitative X-ray microanalysis. Mercury intrusion porosimetry (Pore Master 33, Quantachrome Instruments) was used to determine the pore volume distribution. It is established on the basis that a non-wetting liquid (any with a contact angle superior than 90°) will only intrude into capillaries under pressure. The relationship between the pressure and capillary diameter is described by Washburn [34] as Equation (1):

$$P = \frac{-4 \gamma \cos(\theta)}{d} \quad (1)$$

where P : pressure, γ surface tension of the liquid, θ : contact angle of the liquid, and d : diameter of the capillary. Mercury must be forced using pressure into the pores of a material. The pore-size distribution is determined from the volume intruded at each pressure increment. Total porosity is determined from the total volume intruded.

The bending strength was performed with an Instron 3369 apparatus. The load and loading used speed were 50 kN and 0.1 mm/min, respectively. For this trial, five heated samples were studied.

Filtration tests were conducted on a laboratory microfiltration pilot, using a recycling configuration. The pilot was equipped with two silver wire electrodes used to measure the diffusion potential. The diffusion potential coefficient is defined by the Equation (2) [35]:

$$DP = \frac{\Delta E}{\Delta P} \quad (2)$$

where ΔE : the electric potential between the walls of the membrane and ΔP the applied pressure. The tests were performed at room temperature. The membranes were conditioned by immersion in distilled water for 12 h before the filtration tests. The schematic diagram of the filtration pilot is shown in Figure 2. It was principally composed of a circulation pump, air compressor, feed container of two liters, two manometers, and a membrane model. Transmembrane pressure was variable via a pressure regulator. The filtering surface area was about 24 cm² for all filtration samples. It is worth noting that three membrane samples were employed for filtration tests to obtain the reproducibility of experimental results. Moreover, all filtration experimentations were conducted at room temperature.

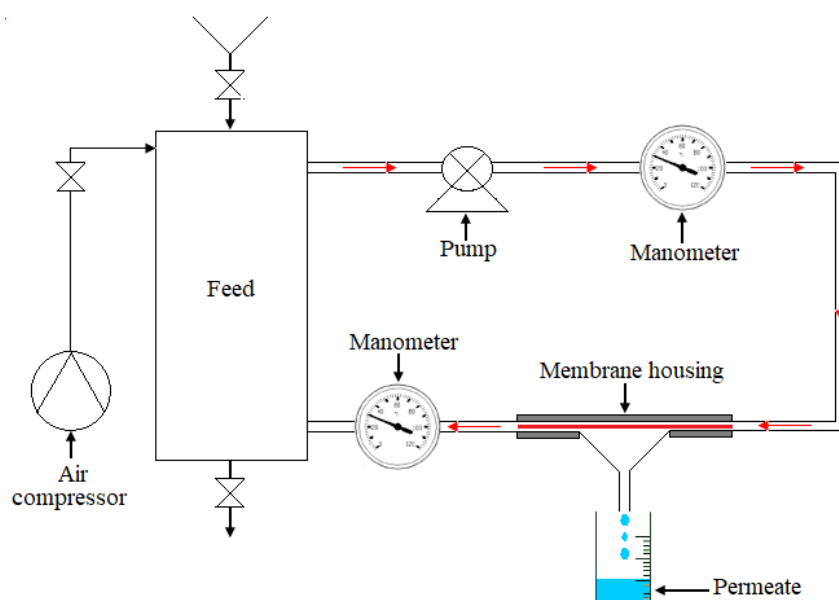


Figure 2. Scheme of the filtration pilot.

The chemical oxygen demand (COD) was determined using a LOVIBOND PCcheckit vario (LOVIBOND, London, UK), which contains a photometer and an ET 108 reactor. 2 mL of samples was mixed with the oxidizing acid solution in a vial that was then held at 150 °C for 2 h. After cooling, the mixed solution was analyzed in the PCcheckit vario photometer.

The biological oxygen demand (BOD) was measured using a LOVIBOND IR-Sensomat containing an IR-pressure-sensor and a stirring system. 500 mL of every sample was kept in a flask in an incubator for 5 days. Variance in air pressure was detected by the IR-sensor and converted directly into mg/L of BOD.

Suspended solids content was measured using a DR2010 portable data logging spectrophotometer (photometric method).

2.3. Experimental Design

The variations of the technological properties (Y_i) of the membranes versus the processing factors (sawdust addition (τ), temperature (T), and soaking time (t)) was assessed using a second-degree polynomial model [16,36,37]. This equation is in the following form:

$$\begin{aligned}
 Y &= a_0 + a_1X_1 + a_2X_2 + a_3X_3 + a_{11}X_1^2 + a_{22}X_2^2 + a_{33}X_3^2 + a_{12}X_1X_2 + a_{13}X_1X_3 \\
 &\quad + a_{23}X_2X_3 \\
 Y &= a_0 + \sum_{i=1}^k a_iX_i + \sum_{i=1}^k a_{ii}X_i^2 + \sum_{i=1}^{k-1} \sum_{j=i+1}^k a_{ij}X_iX_j
 \end{aligned}
 \tag{3}$$

where: X_1 , X_2 and X_3 are the coded variables corresponding to τ , T and t , respectively.

$$X_1 = \frac{\tau - \tau_0}{\Delta\tau}; X_2 = \frac{T - T_0}{\Delta T}; X_3 = \frac{t - t_0}{\Delta t}
 \tag{4}$$

τ_0 , T_0 , and t_0 are the sawdust addition, firing temperature, and soaking time at the centers of the experimental range ($\tau_0 = 12.5$ wt. %, $T_0 = 1000$ °C and $t_0 = 2.5$ h). Δt , ΔT , and $\Delta\tau$ are the variation steps of the considered variables ($\Delta\tau = 7.5$ wt. %, $\Delta T = 100$ °C and $\Delta t = 1.5$ h). a_0 is a constant, and a_1 , a_2 , and a_3 are the weights of the effects of sawdust addition, temperature, and soaking time, respectively. a_{ij} expresses the weight of the interaction effect between i and j factors, and a_{ii} is considered to be a curve-shaped parameter. The coefficients were calculated by Nemrod software using the least-squares regression [38,39]. For this purpose, multiple experiments (16) were performed according to the Dohrlert matrix. The test at the center was multiplied (repeated 3 times) to estimate the experimental error. The experiments proposed by Doehlert matrix and the experimental values of physical properties are shown in Table 2. The accuracy and validity of the used model was confirmed by the analysis of variance (ANOVA) [40–42] represented in Table 3.

Table 2. Experimental design matrix (Doehlert) and measured values of the studied properties. Y_1 : density; Y_2 : firing shrinkage; Y_3 : water absorption; Y_4 : bending strength.

X_1	X_2	X_3	τ (wt. %)	T (°C)	t (h)	Density	Firing Shrinkage	Water Absorption	Bending Strength
						Y_1 (g/cm ³)	Y_2 (%)	Y_3 (%)	Y_4 (MPa)
1	0	0	20.00	1000.00	2.50	2.012	2.010	22.763	1.218
-1	0	0	5.00	1000.00	2.50	2.050	1.050	16.792	1.506
0.5	0.866	0	16.25	1086.60	2.50	2.018	2.677	22.218	1.760
-1	-0.866	0	8.75	913.40	2.50	2.030	0.676	20.429	1.610
0.5	-0.866	0	16.25	913.40	2.50	2.065	2.103	24.497	1.210
-1	0.866	0	8.75	1086.60	2.50	2.100	1.643	18.603	1.970
0.5	0.2887	0.8165	16.25	1028.87	3.72	2.010	2.309	22.938	1.590
-1	-0.289	-0.817	8.75	971.13	1.28	2.077	0.773	18.878	1.680
0.5	-0.289	-0.817	16.25	971.13	1.28	2.140	2.199	23.360	1.480
0	0.5774	-0.817	12.50	1057.74	1.28	2.065	1.633	20.217	1.580
-1	0.2887	0.8165	8.75	1028.87	3.72	2.087	0.883	18.644	1.800
0	-0.577	0.8165	12.50	942.26	3.72	2.040	0.961	22.511	1.300
0	0	0	12.50	1000.00	2.50	2.040	1.537	22.058	1.460
0	0	0	12.50	1000.00	2.50	2.100	1.500	21.980	1.400
0	0	0	12.50	1000.00	2.50	1.990	1.560	22.100	1.470
0	0	0	12.50	1000.00	2.50	2.038	1.56	22.1	1.47

Table 3. Of variance (ANOVA), values of correlation coefficient (R^2) and standard deviations (σ) for the considered responses: Y_1 : density; Y_2 : firing shrinkage; Y_3 : water absorption; Y_4 : bending strength.

	Water Absorption			
	Y_1 (g/cm ³)	Y_2 (%)	Y_3 (%)	Y_4 (MPa)
F-ratio	70.5559	1512.0456	86.5970	350.329
Signification	0.164 **	<0.01 ***	0.205 **	0.0352 ***
R^2	0.98	0.99	0.97	0.96
σ	0.1	0.084	0.15	0.12

*** Statistically significant at the level > 99.9% (probability (p) < 0.001). ** Statistically significant at the level > 99% (p < 0.01).

3. Results and Discussion

3.1. Thermal Transformations and Microstructure of Membranes

3.1.1. Micaceous Clay-Sawdust Mixture (SA-SC)

The X-ray diffraction pattern of the heated materials (Figure 3) showed that hydro-muscovite and dolomite decomposed at $T < 900$ °C. Indeed, hydro-muscovite sheet mica dehydroxylated at $T < 700$ °C and dolomite decomposed in the range 750–880 °C. The Differential thermal analysis (DTA) analysis (Figure 4) supports this results and indicates the occurrence of two peaks at 787 °C and 878 °C corresponding to the decomposition of dolomite in two stages: $(CaMg(CO_3)_2 \rightarrow CaCO_3 + CO_2 + MgO$ and $CaCO_3 \rightarrow CaO + CO_2)$ [43,44]. Quartz resisted heat treatment, but its amount diminished slightly with increasing temperature, likely because it contributed to the neoformation process. Moreover, gehlenite and diopside were detected at 900 °C, likely from the breakdowns of clay mineral (hydro-muscovite) and released lime of carbonate (dolomite) decomposition. As far as the X-ray diffraction was concerned, the amount of gehlenite decreased, and that of diopside increased with increasing temperature, suggesting that the latter developed with further heat treatment. The added pore-forming agent (sawdust) seems not to have influenced the neoformation process in either qualitative or quantitative terms.

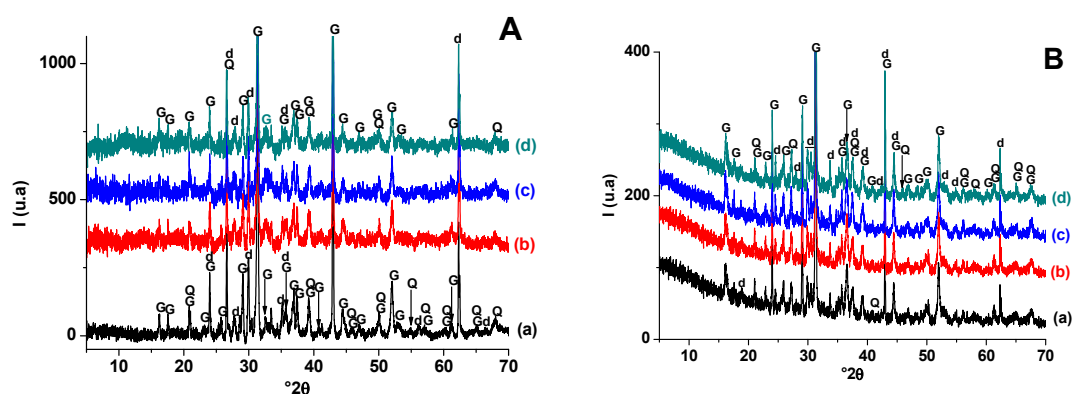


Figure 3. X-ray diffraction patterns of blends heated at 900 °C (A) and 1100 °C (B). (a) SA; (b) SA-SC (5 wt. % of SC); (c) SA-SC (10 wt. % of SC); (d) SA-SC (20 wt. % of SC). G: Gehlenite (PDF # 72-2128); Q: Quartz (PDF # 79-1911); d: diopside (PDF # 75-0945).

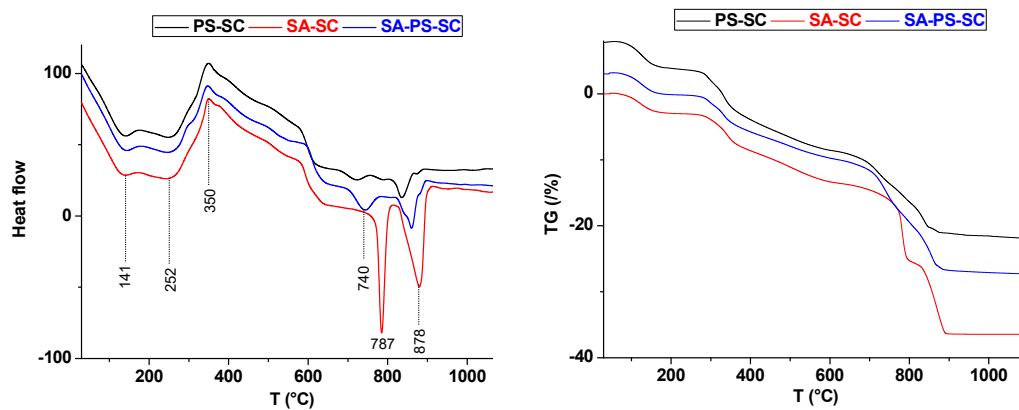


Figure 4. Thermal curves (DTA) and thermogravimetric analysis (TG) of PS-SC, SA-SC and SA-PS-SC.

As a result of heating, the laminated structure detected at low temperature (Figure 5a) disappeared, and agglomerated particles took place at high temperature (Figure 5b). The SEM observations (Figure 5c,d) also revealed grainy particles across the matrix, which corresponded to grains of gehlenite according to Energy Dispersive Spectroscopy (EDS) analysis. Loutou et al. (2013) [8] reported that gehlenite formed as granular particles within pores. These pores appeared to correspond to carbonates sites rich with lime (gehlenite formation source). At high temperature (1100 °C), grainy particles of gehlenite were agglomerated (Figure 5e,f) leading to the coalescence of some pores with the increase of temperature.

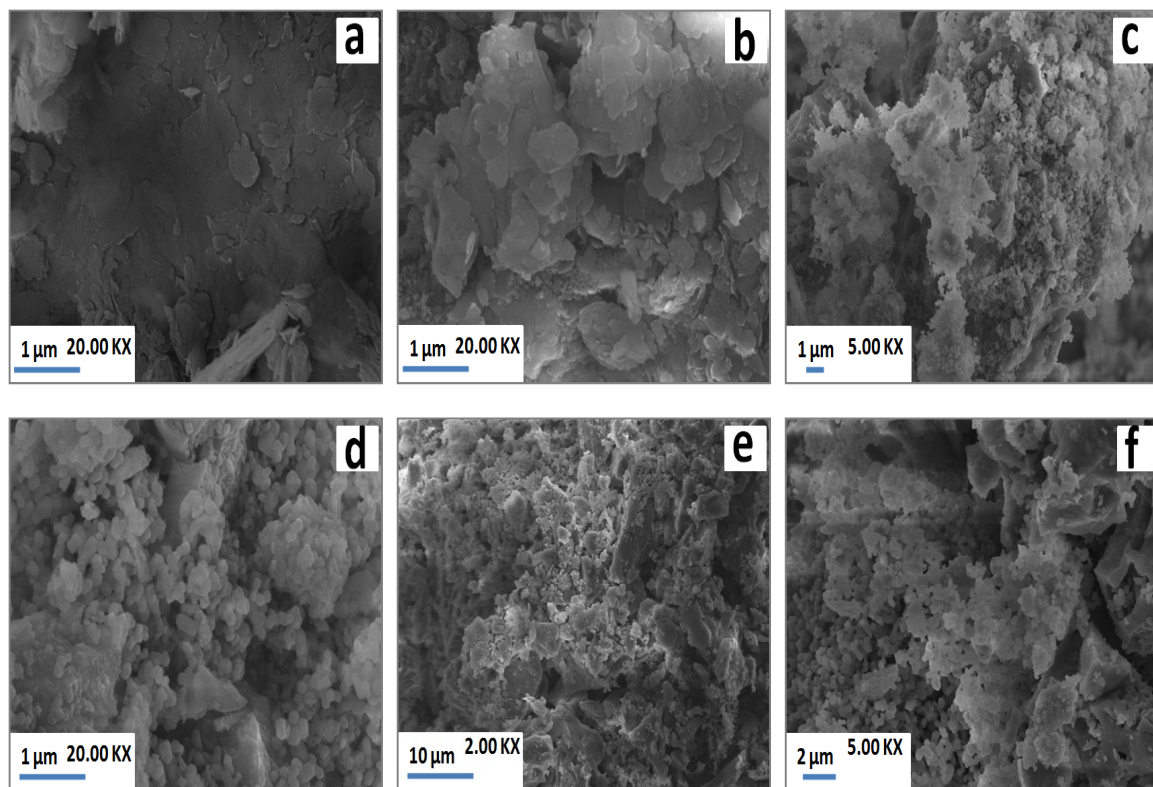


Figure 5. SEM micrographs of PS-SC (20 wt. % of SC) blends heated at 900 °C (a) and 1100 °C (b–f).

3.1.2. Phosphate Sludge-Sawdust Blend (PS-SC)

Referring once again to Figure 4, the thermal analysis (DTA) of PS-SC-fired blends showed that samples experienced four transformations at 141, 252, 730, and 836 °C. These endothermic peaks were attributed respectively to hygroscopic water loss [45], pore additive (sawdust) dehydration, dolomite

first stage decomposition, and calcite decomposition [46,47]. The addition of the sawdust shifted these peaks to a higher temperature. The exothermic peak located at 350 °C was ascribed to sawdust firing, and was accompanied with 1.61% of weight loss (Figure 4).

Taking into consideration the X-ray diffractograms (Figure 6), only quartz and fluorapatite resisted the heat treatment. Their amount decreased with increasing temperature, probably due to the involvement of quartz in the neoformation and the partial fusion of fluorapatite at high temperatures (1100 °C). Gehlenite was the only phase neoformed in all studied PS-SC samples, and its proportion increased at the expense of both quartz and fluorapatite.

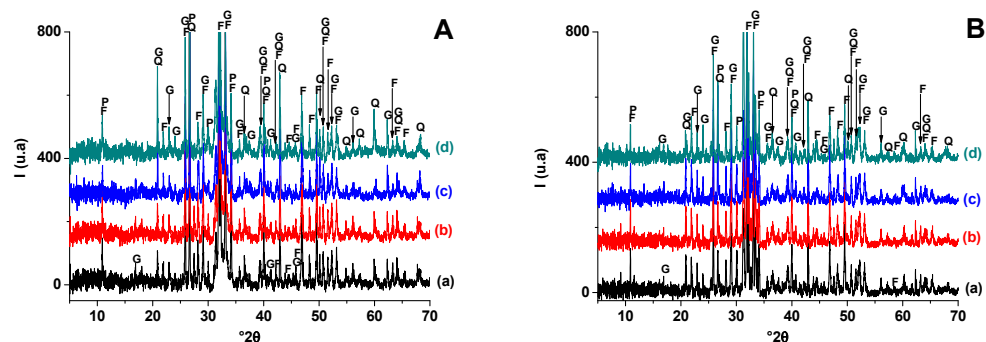


Figure 6. X-ray diffraction patterns of SA-PS (50 wt. % of SA) blends heated at 900 °C (A) and 1100 °C (B). (a) SA-PS; (b) SA-PS-SC (5wt. % of SC); (c) SA-PS-SC (10 wt. % of SC); (d) SA-PS-SC (20 wt. % of SC). G: Gehlenite (PDF # 72-2128); Q: Quartz (PDF # 79-1911); F: Fluorapatite (PDF # 83-0556); P: Calcium phosphates (PDF # 11-0232).

SEM examinations showed certain porosity with isolated particles at low temperature (Figure 7a). Apparently, the latter particles coalesced with the increase of temperature leading to coarse melted blocks throughout the samples (Figure 7b).

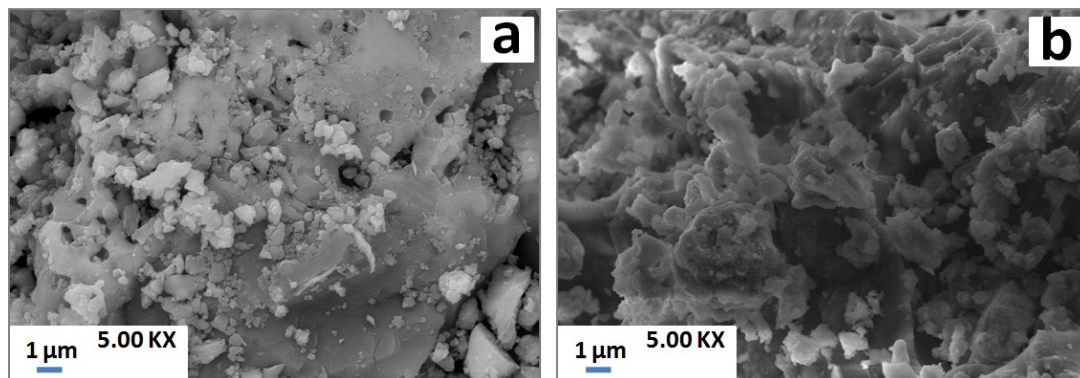


Figure 7. SEM micrographs of PS-SC (20 wt. % of SC) blends heated at 900 °C (a) and 1100 °C (b).

3.1.3. Ternary Mixture (PS-SA-SC)

X-ray diffraction analysis of fired samples (Figure 8.) showed that: (i) quartz and fluorapatite (original minerals) were encountered in all heated samples, but their amounts varied with firing temperature; (ii) hydro-muscovite and carbonate decomposed at $T < 900$ °C; (iii) the addition of the sawdust did not affect phase transformation; (vi) gehlenite and calcium phosphate developed at lower temperature and resisted heating afterwards. Gehlenite was derived from carbonate-released lime and the breakdowns of clay minerals, while calcium phosphate resulted from fluorapatite partial decomposition.

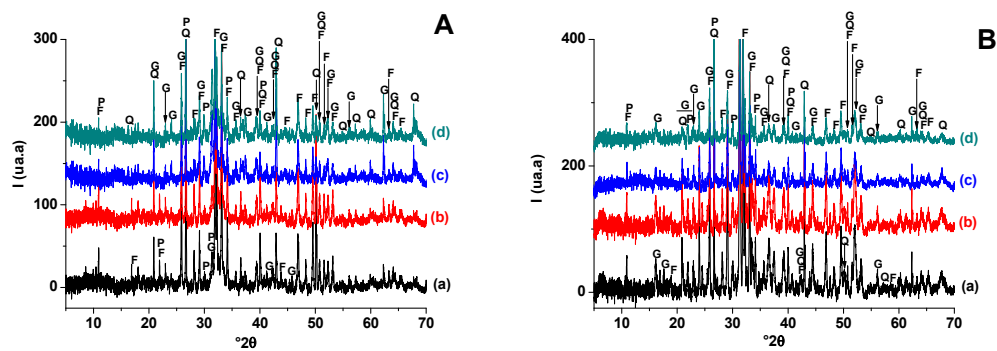


Figure 8. X-ray diffraction patterns of SA-PS (50 wt. % of SA) blends heated at 900 °C (A) and 1100 °C (B). (a) SA-PS; (b) SA-PS-SC (5 wt. % of SC); (c) SA-PS-SC (10 wt. % of SC); (d) SA-PS-SC (20 wt. % of SC). G: Gehlenite (PDF # 72-2128); Q: Quartz (PDF # 79-1911); F: Fluorapatite (PDF # 83-0556); P: Calcium phosphates (PDF # 11-0232).

According to the recorded Thermogravimetric analysis (TGA) curves (Figure 4), two weight losses occurred of about 12.48% and 7.77% between 700 and 880 °C, respectively. In fact, these weight losses consisted of two distinct stages. The first is primary decomposition of dolomite, whereas the second is related to the CO₂ release as a result of calcite decomposition. The weight-loss ratio of the last stage is more prominent.

Due to the heat treatment, grainy structures detected by SEM (Figure 9a) underwent partial melting and thereby contributed to melt formation (Figure 9c). On the other hand, those of gehlenite were agglomerated and was well crystallized (Figure 9b).

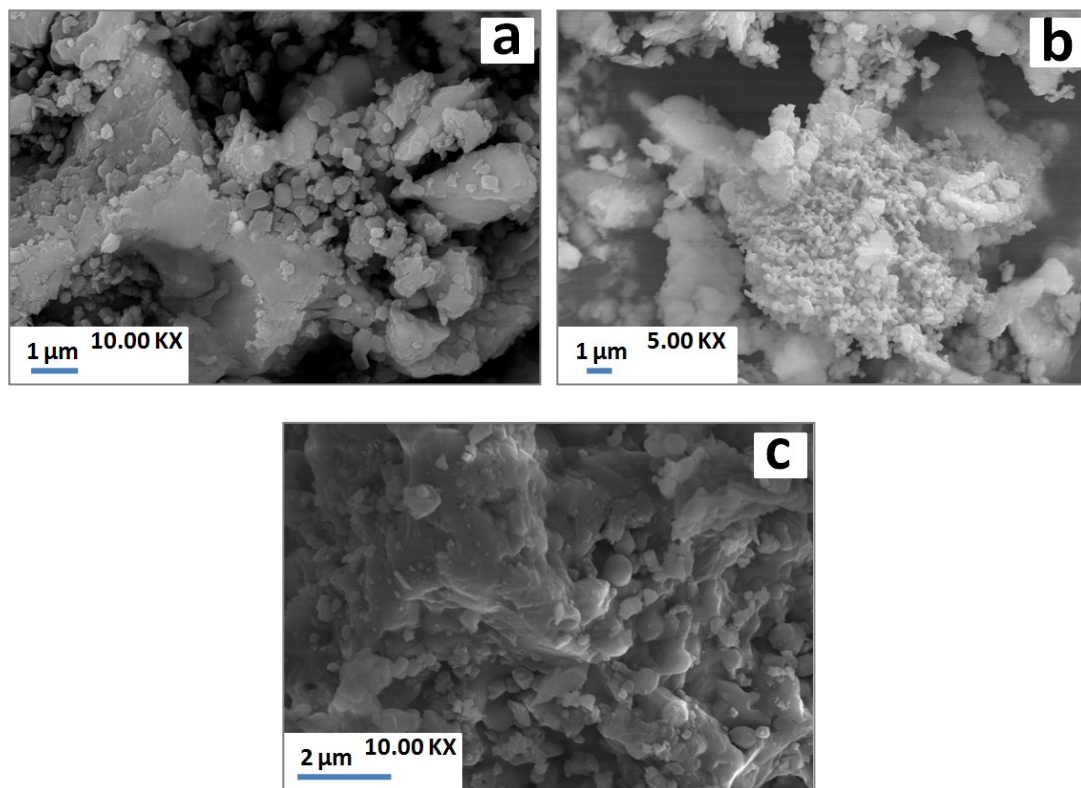


Figure 9. SEM micrographs of SA-PS-SC blends heated at 900 °C (a,b) and 1100 °C (c).

3.2. Porosimetry and Filtration Tests

Membranes prepared at 900 °C were used for filtration tests to keep a certain porosity level and avoid the partial melting of certain constituents at high temperatures.

Results of pore-size distribution (mercury-intruded volume versus pore size), for micaceous clay, phosphate sludge, and the ternary mixtures, are shown in Figure 10. It is revealed that both PS-containing samples (PS-SA and PS-SA-SC) displayed both larger pores (12–7 μm diameter) and lower pores (2–0.2 μm diameter) with a narrow range of distribution, and therefore exposed a marked incremental porosity (50% and 38%) for pores with 10 μm diameter respectively (Figure 10b,c). On the other hand, Figure 10a showed that SA-SC samples were the subject of only micropore formations. An incremental porosity of about 23% corresponding to pores of 0.7 μm diameter. The results obtained for both PS-containing blends is very interesting, since it will help inhibit the membrane resistance against mass transfer, and subsequently increase the filtration performance. It is clear that the pore formation process depends closely on the firing temperature [48,49] and elements liable to form pores (organic additives, carbonates, etc.).

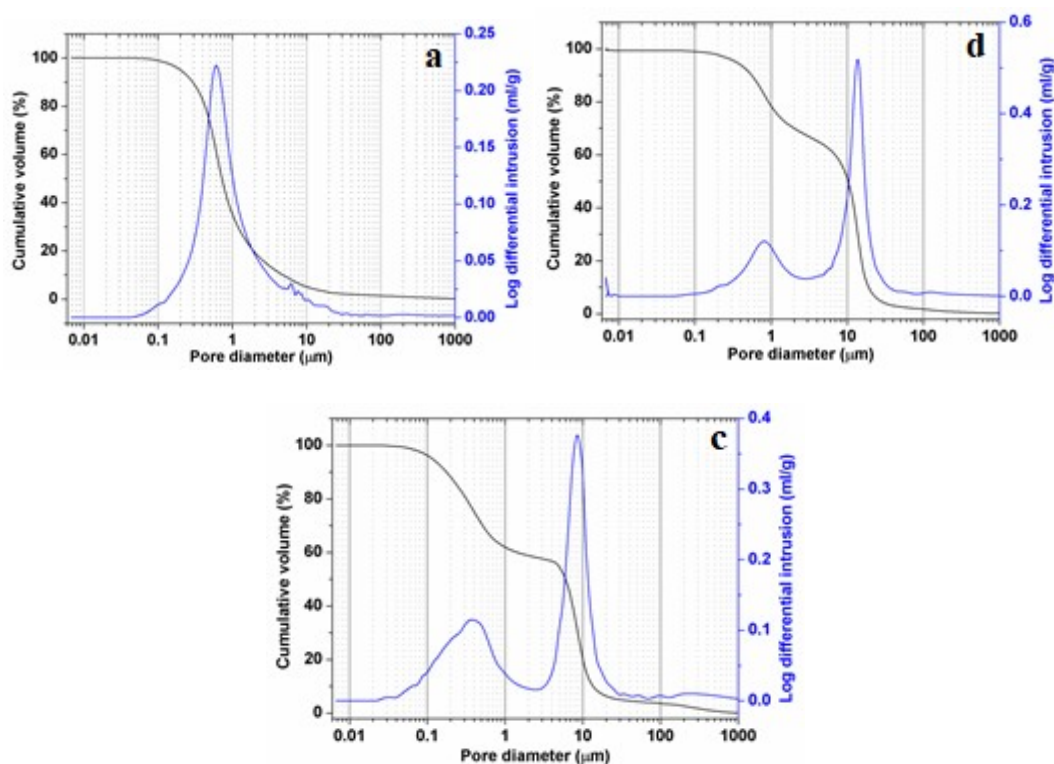


Figure 10. Pore-size distribution from mercury porosimetry of SA-SC blends (a), PS-SC blends (b) and ternary mixture (SA-PS-SC) (c) heated at 900 °C.

The permeability-measuring results from mercury porosimetry are reported in Table 4. Permeability coefficient values showed a marked difference between the behavior of the clay and the phosphate sludge. The coefficients corresponding to the sludge are twice those of clay ($K_{PS}/K_{SA} = 2$). This is probably because the sludge contains more carbonate content (element contributing to pore formation) leading to the occurrence of an additional amount of porosity. These observations also support the role of pore size and the emergence of a reduced tortuous path and further permeability to the water flow in the membrane. The pore morphology also has an effect in this respect, and is to be taken into account.

Table 4. Permeability results from mercury porosimetry (with and/or without tortuosity effect).

Coefficient of Permeability (nm ²)	SA-SC	PS-SC	SA-PS-SC
K _n (Neglecting Tortuosity Effects)	1.2040 × 10 ⁻⁰¹	2.0526 × 10 ⁻⁰¹	1.3857 × 10 ⁻⁰¹
K _t (With Tortuosity Effects)	1.1485 × 10 ⁻⁰¹	2.0158 × 10 ⁻⁰¹	1.3597 × 10 ⁻⁰¹

Variations of the flux versus the transmembrane pressure (Figure 11) showed a nearly linear behavior for all the studied samples. Theoretically, the flux is defined by the following equation:

$$J = L_p \times \Delta P + Cste$$

where *J* is the permeate flux (L/h.m²), *L_p* water permeability (L/h.m².bar), and ΔP the applied transmembrane pressure (bar). The value of the water permeability can be deduced from the slope of the line drawn through the experimental points. It is about 93.89, 68.89, and 52.55 L/h.m².bar for SA-SC, PS-SC, and SA-PS-SC, respectively.

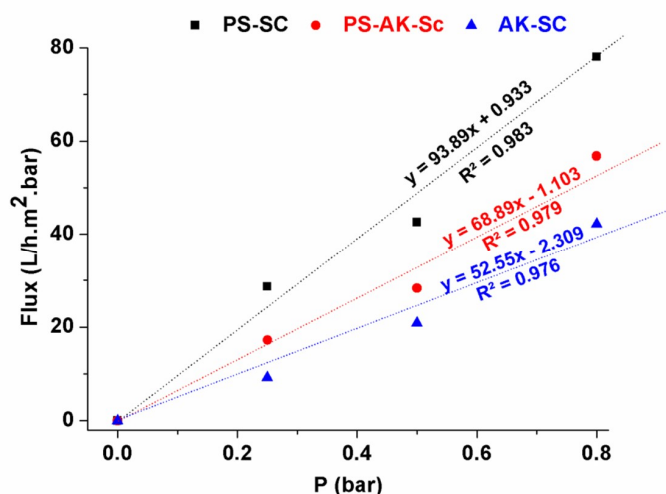


Figure 11. Variation of water flux as a function of transmembrane pressure.

Results of tangential filtration test for textile effluent are represented in Figure 12. It showed the variations of textile effluent permeate with filtration time at a pressure of 0.25 bar. The permeate flux declined continuously during the filtration test for all membranes. This reduction in flow is due essentially to the accumulation of suspended particles onto the membrane surface.

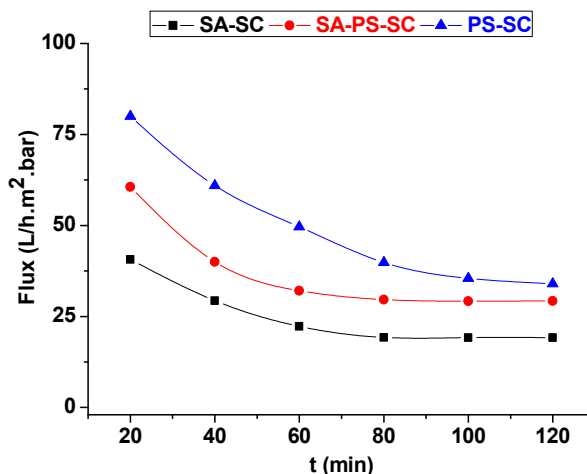


Figure 12. Permeate of textile effluent versus filtration time.

The characterization results of the wastewater samples are reported in mean values (min, max) in Table 4. Filtration suitability was also investigated by assessing the COD present in the industrial wastewater. Generally, the effects resulting from concentration polarization can be minimized but not canceled. In fact, during the movement of the wastewater through the membrane during filtration, particles of different sizes settle on the surface of the membrane. This leads to the formation of a gel-like pseudo-layer. The latter has the effect of reducing the permeate flux due to the increase in hydraulic resistance of the system (as explained before). Depending on the size and/or the structure of the pores, as well as their surface distribution, a total blockage of the flux can occur. Simultaneously with the preceding phenomena, the pseudo-layer often leads to a gradual increase in solutes retention, as can be seen in COD values before and after filtration in Table 4. According to Lopes et al. [50], the performance of a membrane is satisfactory when the COD reduction exceeds 73%. In our case, the COD reduction was in the range 70, 72, and 75%, which corresponds to a COD of 405, 380, and 340 mg/L, respectively. The ternary mixture-based membrane was the only one that fell within the acceptance range. The COD remaining in the filtrate probably came from low-molecular-weight solutes that may have passed through the membrane. It should be noted that COD retention is highly influenced by temperature, transmembrane pressure, and pollutant concentration [50–53].

Similarly, the removal efficiency of total organic carbon (TOC) and BOD were in the range 77–83% and 89–93%, respectively for the studied blends. Of all mixtures, the ternary one exhibited the best measurements.

3.3. Physical Properties and Effect of Processing Factors

Given the limitations to the number of figures, only the SA-PS-SC mixture heated at different temperatures will be treated.

As explained in the experimental procedure section, a Dohler matrix was used for creating the experimental design. The experimental conditions of the planned experiments and the measured properties are given in Table 5.

Table 5. Chemical analyzes of wastewater before and after filtration and comparison with literature values.

Chemical analyzes	Previous Studies (Literature)		Current Study			
	Textile Wastewater	Dyeing Wastewater	Before Filtration	After Filtration		
				PS-SC	SA-SC	PS-SA-SC
pH	5.3–11 ^a	8.7–12.5 ^a	8.3	7.15	6.59	6.79
Conductivity (mS/cm)	2.5–8.5 ^a	2–30 ^a	2.9	1.6	1.4	1.25
COD (mg/L)	330–1550 ^a	280–7900 ^a	1330	380	405	340
TOC (mg/L)	150–390 ^a	-	180	39	43	32
BOD (mg/L)	1350–1910 ^{b,c,d}	18–152 ^{b,c,d}	190	19	21	15
Turbidity (NTU)	36–224 ^{b,c,d}	1.9–153 ^{b,c,d}	211	25	29	18

^a Dilaver et al. (2018) [1]; ^b Qin et al. (2007) [52]; ^c Lopes et al. (2005) [50]; ^d Kadirvelu et al. (2000) [51].

The validity of the model was evaluated by ANOVA [36,37]. The calculated data revealed that significance exceeded 99%, values of the R^2 approached 1, and the Fisher-ratio $\gg 1$. These outcomes attested that the considered model fitted well with the variations of the studied properties versus processing factors.

The equations expressing the change in the density (Y_1), firing shrinkage (Y_2), water absorption (Y_3), and the bending strength (Y_4) according to coded variables, are as follows:

$$Y_1 = 2.084 - 0.018X_1 + 0.001X_2 - 0.03X_3 - 0.01X_1^2 + 0.022X_2^2 + 0.037X_3^2 - 0.07X_1X_2 - 0.057X_1X_3 + 0.49X_2X_3 \quad (5)$$

$$Y_2 = 1.531 + 0.89X_1 + 0.462X_2 - 0.065X_3 - 0.006X_1^2 + 0.318X_2^2 - 0.195X_3^2 - 0.225X_1X_2 + 0.109X_1X_3 + 0.449X_2X_3 \quad (6)$$

$$Y_3 = 22.046 + 3.55X_1 - 1.267X_2 + 0.334X_3 - 2.269X_1^2 - 0.056X_2^2 - 0.851X_3^2 - 0.262X_1X_2 - 0.022X_1X_3 + 0.204X_2X_3 \quad (7)$$

$$Y_4 = 1.443 - 0.2X_1 + 0.254X_2 - 0.01X_3 - 0.081X_1^2 + 0.286X_2^2 + 0.141X_3^2 + 0.11X_1X_2 - 0.045X_1X_3 + 0.409X_2X_3 \quad (8)$$

Examination of linear coefficients values showed that:

- The weights of the effects of the factors studied on the studied properties follows the order: $t > \tau > T$ for density, $\tau > T > t$ for firing shrinkage and water absorption, while for resistance compression, it follows the order $T > \tau > t$.
- Increasing the temperature (T) had a positive effect on all physical properties. In fact, following the increase in temperature, sintering is initiated, and the matrix is consolidated and therefore the mechanical properties are improved.
- The addition of sawdust (τ) had a marked effect on the properties. This effect may be related to the abundance of pores. These were replenished following the decomposition of sawdust, and release CO_2 .
- Increasing the soaking time (t) had a positive effect on the density and the shrinkage firing (Figure 14); however, it adversely affects the other two properties. Probably, the adoption of long soaking time favors diffusion phenomena, which leads to an increase in the amount of gehlenite formed, and thus the porosity.
- The effect of interactions between two experimental factors considered changed according to the property. For example, considering the equation of the bending strength, sawdust addition and time have an antagonistic interaction. In other words, the simultaneous increase of these two factors decreases the mechanical strength (Figure 13). The same happens in the case of firing shrinkage for sawdust rate and temperature factors (Figure 14). However, the interaction between the temperature and the soaking time was synergistic in the case of bending strength. This means that the simultaneous increase of T and t led to the formation of mechanically resistant samples (Figure 13).

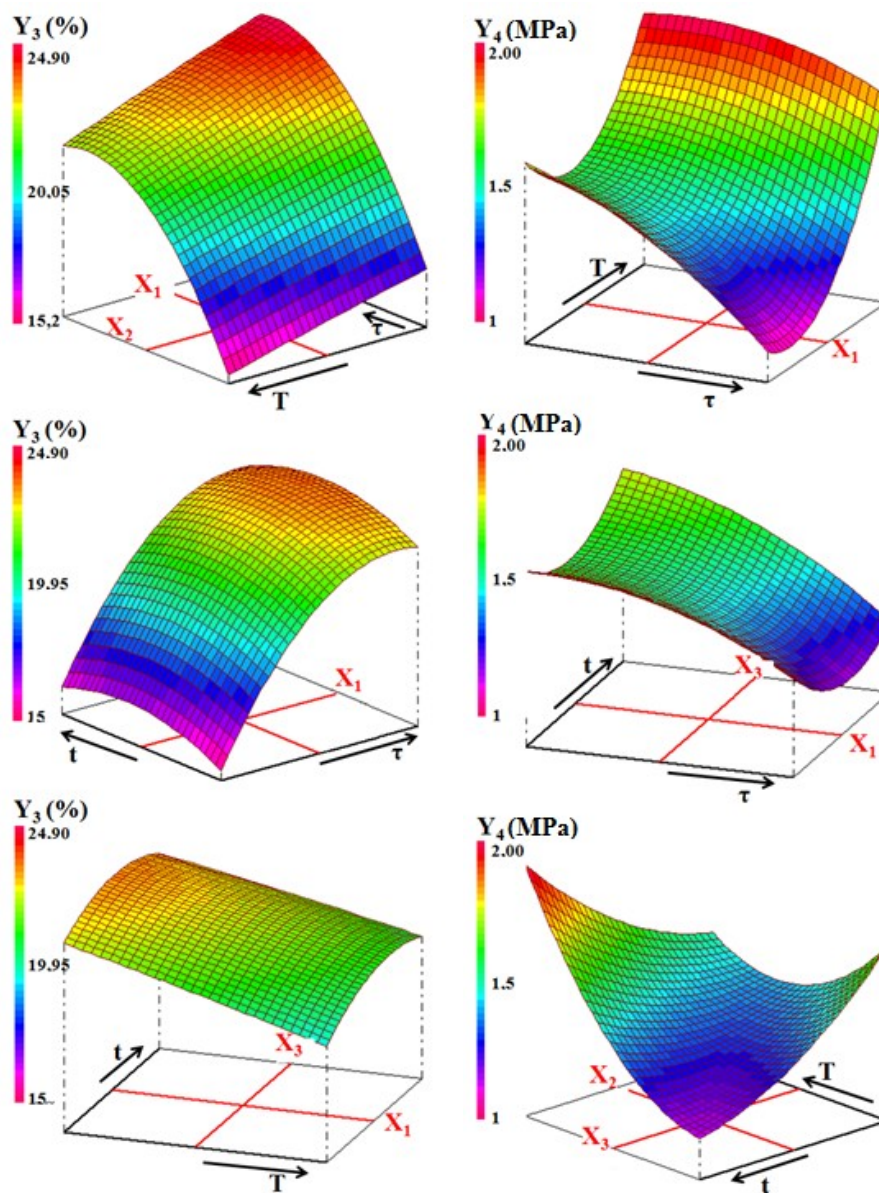


Figure 13. Variation of the water absorption (Y_3) and compressive strength (Y_4) of the ternary blends.

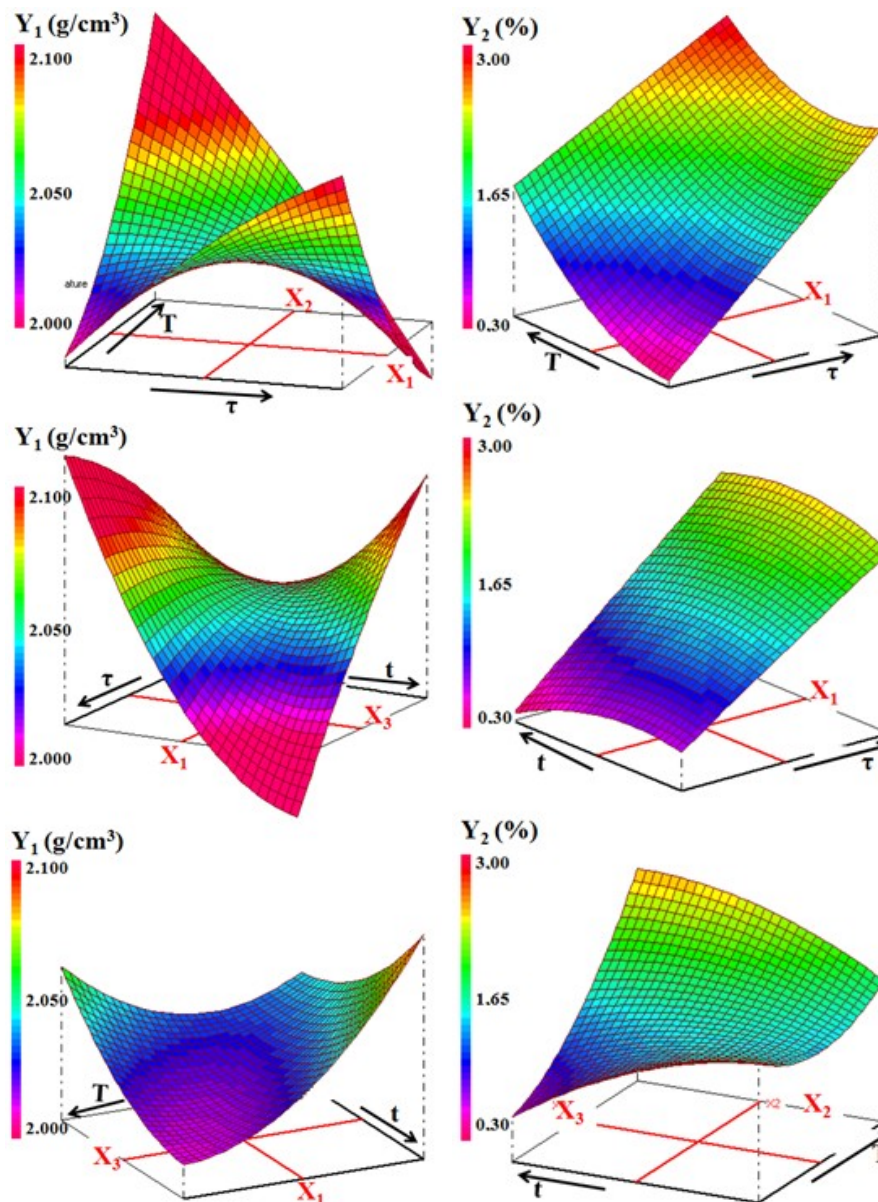


Figure 14. Three-dimensional representation of the variations of density (Y_1) and the firing shrinkage (Y_2) against the processing factors for the ternary mixture.

4. Conclusions

This study reported the manufacturing and the characterization of new ceramic filtration membranes from micaceous clay and phosphate sludge. The results of mineralogical, mechanical, and physical characterizations on the studied materials allowed the conclusions as follows:

- Gehlenite and calcium phosphate neoformed in heated blends containing phosphate sludge (binary and ternary mixture), while the SA-SC mixture was the subject of formation gehlenite and the diopside simultaneously. These neoformed phases were derived from carbonate-released lime and decomposition products of clay minerals.
- It is possible, by adding sawdust, to produce porous bodies.
- The melt formed at high temperature can be connected to the partial melting of fluorapatite.

- Phosphate sludge-based blends showed low mechanical properties (bending strength) compared to clay-based mixtures. That suggests that the incorporation of micaceous clay overcomes this problem because of its high aluminosilicate level.
- The results of filtration tests have shown that the membrane filters based on clay-amended phosphate sludge can be employed in the treatment of textile effluents. In addition, these membrane materials may be used as a carrier of the microfiltration membrane.
- The use of the experimental design allowed assessment of the weight of the effects of experimental factors on the physical properties. Firing temperature and sawdust addition are the most influential factors. Temperature had a positive effect on the studied properties, while sawdust addition has a mitigated effect.

Author Contributions: Conceptualization, M.L.; Data curation, M.L. and W.M.; Formal analysis, M.L., M.K., M.M., L.G. and C.F.; Funding acquisition, R.H.; Investigation, M.L. and M.K.; Methodology, M.L. and R.H.; Project administration, R.H.; Resources, L.G. and Y.T.; Software, M.L. and W.M.; Supervision, M.M., C.F. and R.H.; Validation, M.L.; Writing—original draft, M.L.; Writing—review & editing, R.H.

Funding: This research received no external funding.

Acknowledgments: This work was supported in part by the Erasmus Mundus Program (BATTUTA). Special thanks to the Moroccan Center for Analysis and Characterization (CAC) associated with Cadi Ayyad University (UCA), for helping in some sample characterization.

Conflicts of Interest: The authors declare no conflict of interest.

References

1. Dilaver, M.; Hocaoglu, S.M.; Soydemir, G.; Dursun, M.; Keskinler, B.; Koyuncu, İ.; Ağtaş, M. Hot wastewater recovery by using ceramic membrane ultrafiltration and its reusability in textile industry. *J. Clean. Prod.* **2018**, *171*, 220–233. [[CrossRef](#)]
2. Guo, Y.; Song, Z.; Xu, B.; Li, Y.; Qi, F.; Croue, J.-P.; Yuan, D. A novel catalytic ceramic membrane fabricated with CuMn2O4 particles for emerging UV absorbers degradation from aqueous and membrane fouling elimination. *J. Hazard. Mater.* **2018**, *344*, 1229–1239. [[CrossRef](#)] [[PubMed](#)]
3. Palacio, L.; Bouzerdi, Y.; Ouammou, M.; Albizane, A.; Bennazha, J.; Hernández, A.; Calvo, J.I. Ceramic membranes from Moroccan natural clay and phosphate for industrial water treatment. *Desalination* **2009**, *245*, 501–507. [[CrossRef](#)]
4. Stylianou, S.K.; Katsoyiannis, I.A.; Mitrakas, M.; Zouboulis, A.I. Application of a ceramic membrane contacting process for ozone and peroxone treatment of micropollutant contaminated surface water. *J. Hazard. Mater.* **2018**, *358*, 129–135. [[CrossRef](#)] [[PubMed](#)]
5. Torres, J.J.; Rodriguez, N.E.; Arana, J.T.; Ochoa, N.A.; Marchese, J.; Pagliero, C. Ultrafiltration polymeric membranes for the purification of biodiesel from ethanol. *J. Clean. Prod.* **2017**, *141*, 641–647. [[CrossRef](#)]
6. Dong, Y.; Ma, L.; Tang, C.Y.; Yang, F.; Quan, X.; Jassby, D.; Zaworotko, M.J.; Guiver, M.D. Stable Superhydrophobic Ceramic-Based Carbon Nanotube Composite Desalination Membranes. *Nano Lett.* **2018**, *18*, 5514–5521. [[CrossRef](#)]
7. Loutou, M.; Hajjaji, M.; Babram, M.A.; Mansori, M.; Favotto, C.; Hakkou, R. Phosphate sludge-based ceramics: Microstructure and effects of processing factors. *J. Build. Eng.* **2017**, *11*, 48–55. [[CrossRef](#)]
8. Loutou, M.; Hajjaji, M.; Mansori, M.; Favotto, C.; Hakkou, R. Phosphate sludge: Thermal transformation and use as lightweight aggregate material. *J. Environ. Manag.* **2013**, *130*, 354–360. [[CrossRef](#)]
9. Chrysochoou, M.; Dermatas, D.; Grubb, D.G. Phosphate application to firing range soils for Pb immobilization: The unclear role of phosphate. *J. Hazard. Mater.* **2007**, *144*, 1–14. [[CrossRef](#)] [[PubMed](#)]
10. Yin, H.; Yun, Y.; Zhang, Y.; Fan, C. Phosphate removal from wastewaters by a naturally occurring, calcium-rich sepiolite. *J. Hazard. Mater.* **2011**, *198*, 362–369. [[CrossRef](#)]
11. Lath, S.; Knight, E.R.; Navarro, D.A.; Kookana, R.S.; McLaughlin, M.J. Sorption of PFOA onto different laboratory materials: Filter membranes and centrifuge tubes. *Chemosphere* **2019**, *222*, 671–678. [[CrossRef](#)]
12. Roussanaly, S.; Anantharaman, R.; Lindqvist, K.; Hagen, B. A new approach to the identification of high-potential materials for cost-efficient membrane-based post-combustion CO₂ capture. *Sustain. Energy Fuels* **2018**, *2*, 1225–1243. [[CrossRef](#)]

13. Abbasi, M.; Mirfendereski, M.; Nikbakht, M.; Golshenas, M.; Mohammadi, T. Performance study of mullite and mullite–alumina ceramic MF membranes for oily wastewaters treatment. *Desalination* **2010**, *259*, 169–178. [[CrossRef](#)]
14. Wan, W.; Zhang, R.; Ma, M.; Zhou, Y. Monolithic aerogel photocatalysts: a review. *J. Mater. Chem. A* **2018**, *6*, 754–775. [[CrossRef](#)]
15. Fontes, W.C.; Franco de Carvalho, J.M.; Andrade, L.C.R.; Segadães, A.M.; Peixoto, R.A.F. Assessment of the use potential of iron ore tailings in the manufacture of ceramic tiles: From tailings-dams to “brown porcelain”. *Constr. Build. Mater.* **2019**, *206*, 111–121. [[CrossRef](#)]
16. Loutou, M.; Hajjaji, M.; Mansori, M.; Favotto, C.; Hakkou, R. Heated blends of clay and phosphate sludge: Microstructure and physical properties. *J. Asian Ceram. Soc.* **2016**, *4*, 11–18. [[CrossRef](#)]
17. Loutou, M.; Hajjaji, M.; Mansori, M.; Favotto, C.; Hakkou, R. Heated blends of phosphate waste: Microstructure characterization, effects of processing factors and use as a phosphorus source for alfalfa growth. *J. Environ. Manag.* **2016**, *177*, 169–176. [[CrossRef](#)]
18. Loutou, M.; Hajjaji, M. Clayey wastes-based lightweight aggregates: Heating transformations and physical/mechanical properties. *Appl. Clay Sci.* **2017**, *150*, 56–62. [[CrossRef](#)]
19. Kang, D.-Y.; Lydon, M.E.; Yucelen, G.I.; Jones, C.W.; Nair, S. Inside Cover: Solution-Processed Ultrathin Aluminosilicate Nanotube–Poly(vinyl alcohol) Composite Membranes with Partial Alignment of Nanotubes (ChemNanoMat 2/2015). *ChemNanoMat* **2015**, *1*, 70. [[CrossRef](#)]
20. Lü, Q.; Dong, X.; Zhu, Z.; Dong, Y. Environment-oriented low-cost porous mullite ceramic membrane supports fabricated from coal gangue and bauxite. *J. Hazard. Mater.* **2014**, *273*, 136–145. [[CrossRef](#)]
21. Rasouli, Y.; Abbasi, M.; Hashemifard, S.A. Investigation of in-line coagulation-MF hybrid process for oily wastewater treatment by using novel ceramic membranes. *J. Clean. Prod.* **2017**, *161*, 545–559. [[CrossRef](#)]
22. Silva, R.V.; de Brito, J.; Lye, C.Q.; Dhir, R.K. The role of glass waste in the production of ceramic-based products and other applications: A review. *J. Clean. Prod.* **2017**, *167*, 346–364. [[CrossRef](#)]
23. Almandoz, M.C.; Pagliero, C.L.; Ochoa, N.A.; Marchese, J. Composite ceramic membranes from natural aluminosilicates for microfiltration applications. *Ceram. Int.* **2015**, *41*, 5621–5633. [[CrossRef](#)]
24. Qiu, H.; Jiang, J.; Peng, L.; Liu, H.; Gu, X. Choline chloride templated CHA zeolite membranes for solvents dehydration with improved acid stability. *Microporous Mesoporous Mater.* **2019**, *284*, 170–176. [[CrossRef](#)]
25. Funk, J.E.; Dinger, D.R. *Predictive Process Control of Crowded Particulate Suspensions: Applied to Ceramic Manufacturing*; Springer Science & Business Media: Berlin, Germany, 2013; ISBN 978-1-4615-3118-0.
26. Fernandes, H.R.; Tulyaganov, D.U.; Ferreira, J.M.F. Preparation and characterization of foams from sheet glass and fly ash using carbonates as foaming agents. *Ceram. Int.* **2009**, *35*, 229–235. [[CrossRef](#)]
27. Živcová, Z.; Gregorová, E.; Pabst, W.; Smith, D.S.; Michot, A.; Poulier, C. Thermal conductivity of porous alumina ceramics prepared using starch as a pore-forming agent. *J. Eur. Ceram. Soc.* **2009**, *29*, 347–353. [[CrossRef](#)]
28. Živcová, Z.; Černý, M.; Pabst, W.; Gregorová, E. Elastic properties of porous oxide ceramics prepared using starch as a pore-forming agent. *J. Eur. Ceram. Soc.* **2009**, *29*, 2765–2771. [[CrossRef](#)]
29. Cao, J.; Rambo, C.R.; Sieber, H. Preparation of Porous Al₂O₃-Ceramics by Biotemplating of Wood. *J. Porous Mater.* **2004**, *11*, 163–172. [[CrossRef](#)]
30. Sutcu, M.; Akkurt, S. The use of recycled paper processing residues in making porous brick with reduced thermal conductivity. *Ceram. Int.* **2009**, *35*, 2625–2631. [[CrossRef](#)]
31. Bose, S.; Das, C. Sawdust: From wood waste to pore-former in the fabrication of ceramic membrane. *Ceram. Int.* **2015**, *41*, 4070–4079. [[CrossRef](#)]
32. Sutcu, M.; Akkurt, S.; Bayram, A.; Uluca, U. Production of anorthite refractory insulating firebrick from mixtures of clay and recycled paper waste with sawdust addition. *Ceram. Int.* **2012**, *38*, 1033–1041. [[CrossRef](#)]
33. Eliche-Quesada, D.; Corpas-Iglesias, F.A.; Pérez-Villarejo, L.; Iglesias-Godino, F.J. Recycling of sawdust, spent earth from oil filtration, compost and marble residues for brick manufacturing. *Constr. Build. Mater.* **2012**, *34*, 275–284. [[CrossRef](#)]
34. Cook, R.A.; Hover, K.C. Mercury porosimetry of hardened cement pastes. *Cem. Concr. Res.* **1999**, *29*, 933–943. [[CrossRef](#)]

35. Saffaj, N.; Persin, M.; Younsi, S.A.; Albizane, A.; Cretin, M.; Larbot, A. Elaboration and characterization of microfiltration and ultrafiltration membranes deposited on raw support prepared from natural Moroccan clay: Application to filtration of solution containing dyes and salts. *Appl. Clay Sci.* **2006**, *31*, 110–119. [[CrossRef](#)]
36. Mora-Tamez, L.; Barim, G.; Downes, C.; Williamson, E.M.; Habas, S.E.; Brutchey, R.L. Controlled Design of Phase- and Size-Tunable Monodisperse Ni₂P Nanoparticles in a Phosphonium-Based Ionic Liquid through Response Surface Methodology. *Chem. Mater.* **2019**, *31*, 1552–1560. [[CrossRef](#)]
37. Njoya, D.; Hajjaji, M. Quantification of the effects of manufacturing factors on ceramic properties using full factorial design. *J. Asian Ceram. Soc.* **2015**, *3*, 32–37. [[CrossRef](#)]
38. Pińkowska, H.; Krzywonos, M.; Wolak, P.; Złocińska, A. Pectin and Neutral Monosaccharides Production during the Simultaneous Hydrothermal Extraction of Waste Biomass from Refining of Sugar—Optimization with the Use of Doehlert Design. *Molecules* **2019**, *24*, 472. [[CrossRef](#)]
39. Ben Khalifa, E.; Rzig, B.; Chakroun, R.; Nouagui, H.; Hamrouni, B. Application of response surface methodology for chromium removal by adsorption on low-cost biosorbent. *Chemom. Intell. Lab. Syst.* **2019**, *189*, 18–26. [[CrossRef](#)]
40. Yurekli, Y.; Yildirim, M.; Aydin, L.; Savran, M. Filtration and removal performances of membrane adsorbers. *J. Hazard. Mater.* **2017**, *332*, 33–41. [[CrossRef](#)] [[PubMed](#)]
41. Šereš, Z.; Maravić, N.; Takači, A.; Nikolić, I.; Šoronja-Simović, D.; Jokić, A.; Hodur, C. Treatment of vegetable oil refinery wastewater using alumina ceramic membrane: optimization using response surface methodology. *J. Clean. Prod.* **2016**, *112*, 3132–3137. [[CrossRef](#)]
42. Vatanpour, V.; Karami, A.; Sheydaei, M. Improved visible photocatalytic activity of TiO₂ nanoparticles to use in submerged membrane photoreactor for organic pollutant degradation. *Int. J. Environ. Sci. Technol.* **2019**, *16*, 2405–2414. [[CrossRef](#)]
43. Valverde, J.M.; Perejon, A.; Medina, S.; Perez-Maqueda, L.A. Thermal decomposition of dolomite under CO₂: insights from TGA and in situ XRD analysis. *Phys. Chem. Chem. Phys.* **2015**, *17*, 30162–30176. [[CrossRef](#)]
44. Gunasekaran, S.; Anbalagan, G. Thermal decomposition of natural dolomite. *Bull. Mater. Sci.* **2007**, *30*, 339–344. [[CrossRef](#)]
45. Eliche-Quesada, D.; Martínez-Martínez, S.; Pérez-Villarejo, L.; Iglesias-Godino, F.J.; Martínez-García, C.; Corpas-Iglesias, F.A. Valorization of biodiesel production residues in making porous clay brick. *Fuel Process. Technol.* **2012**, *103*, 166–173. [[CrossRef](#)]
46. Xie, J.; Chen, T.; Xing, B.; Liu, H.; Xie, Q.; Li, H.; Wu, Y. The thermochemical activity of dolomite occurred in dolomite–palygorskite. *Appl. Clay Sci.* **2016**, *119*, 42–48. [[CrossRef](#)]
47. Qian, H.; Kai, W.; Hongde, X. A novel perspective of dolomite decomposition: Elementary reactions analysis by thermogravimetric mass spectrometry. *Thermochim. Acta* **2019**, *676*, 47–51. [[CrossRef](#)]
48. Rahaman, M.N. *Ceramic Processing*; CRC Press: Boca Raton, FL, USA, 2017; ISBN 978-1-315-15716-0.
49. Studart, A.R.; Gonzenbach, U.T.; Tervoort, E.; Gauckler, L.J. Processing Routes to Macroporous Ceramics: A Review. *J. Am. Ceram. Soc.* **2006**, *89*, 1771–1789. [[CrossRef](#)]
50. Lopes, C.N.; Petrus, J.C.C.; Riella, H.G. Color and COD retention by nanofiltration membranes. *Desalination* **2005**, *172*, 77–83. [[CrossRef](#)]
51. Kadirvelu, K.; Palanival, M.; Kalpana, R.; Rajeswari, S. Activated carbon from an agricultural by-product, for the treatment of dyeing industry wastewater. *Bioresour. Technol.* **2000**, *74*, 263–265. [[CrossRef](#)]
52. Qin, J.-J.; Oo, M.H.; Kekre, K.A. Nanofiltration for recovering wastewater from a specific dyeing facility. *Sep. Purif. Technol.* **2007**, *56*, 199–203. [[CrossRef](#)]
53. Van der Bruggen, B.; Daems, B.; Wilms, D.; Vandecasteele, C. Mechanisms of retention and flux decline for the nanofiltration of dye baths from the textile industry. *Sep. Purif. Technol.* **2001**, *22–23*, 519–528. [[CrossRef](#)]

